Influence of Frictional Melt on the Seismic Cycle: Insights from Experiments on Rock Analog Material

E. M. Conrad[1, 2], N. Tisato[2], B. M. Carpenter[3], G. Di Toro[4, 5]

[1] Institute for Geophysics, Jackson School of Geosciences, University of Texas at Austin, Austin, TX, USA.

[2] Department of Geological Sciences, Jackson School of Geosciences, University of Texas at Austin, Austin, TX, USA.

[3] School of Geosciences, University of Oklahoma, Norman, OK, USA.

[4] Dipartimento di Geoscienze, Università degli Studi Padova, 35137 Padua, Italy.

[5] Istituto Nazionale di Geofisica e Vulcanologia, 00143 Rome, Italy.

Corresponding author: Ethan M. Conrad (econrad@utexas.edu)

Key Points:

- We use a newly conceived Energy Controlled Rotary (ECoR) apparatus on polymethyl methacrylate (PMMA) to investigate the seismic cycle in the presence of melts
- Energy flux pulses from the machine to the fault yield fault weakening (flash melting + lubrication) and strengthening (viscous braking)
- Distinct acoustic emission signals correlate with the activation of coseismic fault weakening/strengthening mechanisms

Abstract

The formation of frictional melt likely impacts the coseismic and, when solidified (pseudotachylytes), the interseismic strength of faults. Here we investigate these effects through experiments using a new energy-controlled rotary shear machine (ECoR) on simulated faults made of a transparent rock analog material (polymethyl-methacrylate). As in nature, ECoR allows (1) elastic strain energy to accumulate at different loading rates and (2) the spontaneous nucleation of slip events. ECoR is equipped with a high-speed camera, thermocouples, and transducers to monitor the surface, temperature, and acoustic emissions (AEs), respectively. We perform experiments at normal stresses of ~3.5 MPa across loading rates from 0.15 MPa/s, phase A, to 2.5 MPa/s, phases B-C-D. In phase A, the temperature remains constant, and slip events occur without visible melting every 3.3-6.4 s with 0.5-0.7 MPa stress drops and 3-7 mm displacements. In phases B-C, slip events occur in the presence of melts every 0.5–0.9 s, and the bulk temperature increases progressively. Melt solidification increases static friction yielding slip events with stress drops up to 5 MPa and displacements up to 3 cm. Samples produce high-frequency AEs during slip acceleration and deceleration. Once the bulk temperature reaches ~110ºC, a “final” and silent long displacement event occurs in the presence of melts (Phase D). Experimental observations suggest that melt formation modulates the coseismic (flash melting, melt lubrication, and viscous braking) and interseismic (welding) stages. Furthermore, AEs associated with coseismic fault weakening and strengthening may have their natural equivalent and could be observed in seismograms through near-fault instrumentation.

Plain Language Summary

During an earthquake, along faults at depth rocks slide against each other resulting in frictional heat. In some cases, enough heat can be generated that rocks melt influencing the earthquake magnitude and, once melt is solidified, the frequency of successive earthquakes. To investigate these effects and understand more about earthquake behavior during sliding, we performed experiments with a newly devised laboratory machine. We tested a rock-analog material called polymethyl methacrylate glass (commercial name, Plexiglas®). The mechanical behavior of this plastic can be similar to rocks and is simple to use. The experimental apparatus reproduces the natural earthquake cycle by first compressesing two cylinders (top and bottom sample) along the vertical direction and then gradually loads a spring. The spring applies a shear force in the

horizontal direction where the two samples meet. When the spring is loaded, it overcomes a threshold in shear force that depends on the samples conditions. While maintaing the vertical force, spontaneous slip events occur, and the bottom sample spins, rubbing against the locked-in-place top sample. Such a process mimics an earthquake along a fault at depth generating heat. From these experiments we find that during slip frictional melts lubricate the fault at the onset of slip and later act as a viscous brake during slip deceleration and arrest. Moreover, the solidification of frictional melts increases the fault strength leading to higher magnitude successive earthquakes. We used acoustic sensors to monitor the sound and vibrational waves emitted from a slip event. Such vibrations are analog to earthquakes and reveal the occurrence and timing of the processes happening during fault slip. As earthquake monitoring technology improves, the sound waves characteristic of these processes may become evident also in seismograms of natural earthquakes helping to understand how earthquakes work.

1 Introduction

High velocity laboratory rock friction experiments show that thermally controlled mechanisms may play a role in modulating the strength of crustal faults (Di Toro et al., 2011; Niemeijer et al., 2012; Tullis, 2015). Examples include thermal and mechanical pressurization of fluids (e.g., Violay et al., 2015; Badt et al., 2020; Faulkner et al., 2018; Aretusini et al., 2021), frictional melting (e.g., Del Gaudio et al., 2009; Di Toro et al., 2011; Hirose & Shimamoto, 2005; Nielsen et al., 2008, 2010; Niemeijer et al., 2012; Passelègue et al., 2016; Spray, 2005), and flash heating and weakening (e.g., Barbery et al., 2021; Beeler et al., 2008; Goldsby & Tullis, 2011; Rice, 2006; Tisato et al., 2012). This notion is grounded on the hypothesis that a considerable part (~70%) of the earthquake's energy budget is dissipated into heat by frictional resistance along the fault interface (Kanamori & Brodsky, 2004).

The formation of frictional melts along faults (pseudotachylyte once solidified) in the lithosphere represents an extreme scenario of coseismic frictional heat dissipation (Sibson, 1975; Spray, 1995; Scambelluri et al., 2017). Flash heating and weakening control the discontinuous formation of melt at the asperity scale (~mm), induces fault weakening (Hirose & Shimamoto, 2005; Rice, 2006; Violay et al., 2014), and may be followed by the development of a continuous melt layer lubricating the fault (Di Toro et al., 2006; Hirose & Shimamoto, 2005; Spray, 1995).

Instead, during seismic slip deceleration and fault cooling, the increased viscosity of the melt and the melt-glass transition lead to fault restrengthening (Del Gaudio et al., 2009; Lavallée et al., 2015; Violay et al., 2019). The post-seismic slip cooling of the melt into pseudotachylyte may weld the fault, especially in crystalline basement rocks (Di Toro & Pennacchioni, 2005; Mitchell et al., 2016; Proctor & Lockner, 2016).

In rocks exhumed from the lower crust and upper mantle, pseudotachylytes are often found in association with high-temperature mylonites (e.g., Jiang et al., 2015; Passchier et al., 1991; Pennacchioni & Cesare, 1997; Pittarello et al., 2012; Sibson, 1980; Ueda et al., 2008). These observations suggest that pseudotachylytes may form because of the downward propagation of seismic ruptures from the upper to the lower crust or due to shear instabilities in generally ductile regimes at temperatures from 600ºC to 800ºC (Kelemen & Hirth, 2007; Newman et al., 1999). Under these conditions, melt-forming instabilities develop when the interaction between strain-softening behavior and the elastic stiffness of the system is favorable to rapidly release high amounts of stored elastic strain energy (Hobbs et al., 1986). However, the exact nature of the development of such instabilities is uncertain. Intriguingly, fault instabilities associated with the formation of friction melts have also been proposed to explain the intermittent extrusion of lava domes (Kendrick et al., 2014).

While the formation of frictional melts may impact the seismic cycle, our understanding of the influence of these melts and their solidified products over the lifetime of a fault is limited. To address this, we present experiments with a newly conceived energy-controlled rotary shear machine (ECoR) on simulated faults made of polymethyl methacrylate (PMMA) glass. The experimental configuration enables the simulation of seismic cycles producing spontaneous coseismic slip events from which we investigate the evolution of fault strength in the presence of frictional melts. In particular, mechanical, temperature, and acoustic emissions (AEs) data, high frame rate (HFR) digital recordings, and microstructural observations allow us to investigate how: 1) fault strength evolves over seismic cycles with increased fault temperature and melt production,

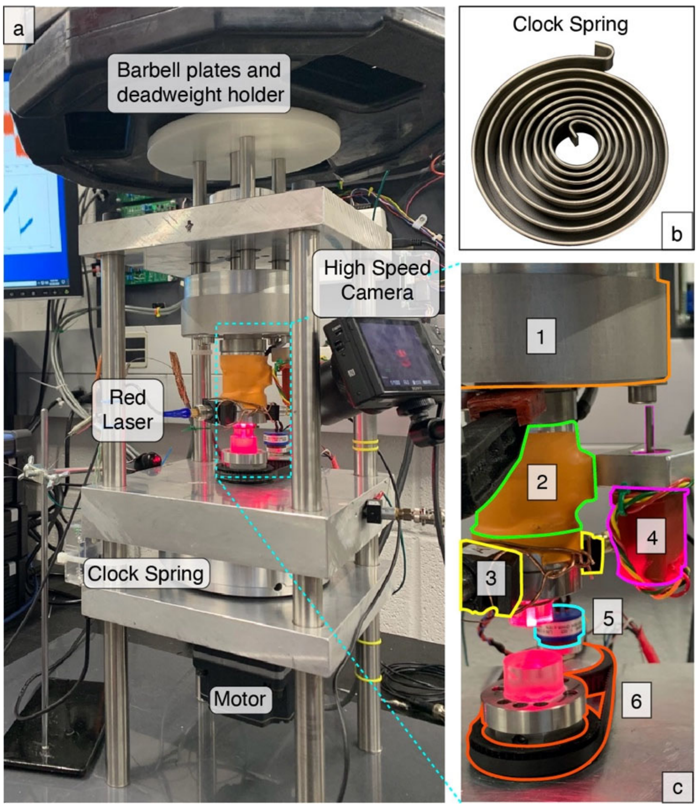

Figure 1: *The energy-controlled rotary shear machine (ECoR). **(a)** Barbell plates loaded to a deadweight holder apply the normal load to the sample. The structural evolution of the slip zone is captured with a high-speed camera recording at 960 fps. The sample is illuminated with a red laser for better optics and to differentiate between air and solid and melted PMMA. A clock spring loaded by a brushless motor applies a linearly increasing torque to the sample. **(b)** The clock spring used in this experiment (spring constant, k = 0.0119 Nm/deg). **(c)** Magnified view of the sample holder assembly. The normal load and torque are measured with a load cell (1) and torque cell (2), respectively. Vertical displacement is measured with a plunger type potentiometer (4). Two acoustic emissions sensors capture the emitted soundwaves (3). A third acoustic emissions sensor is mounted to the side of the machine (out of view). Sample displacement is measured with a rotational potentiometer (5) attached to a pulley system (6).*

2) the energy flux to the fault is related to fault weakening and strengthening during individual slip events (i.e., melt lubrication vs. viscous braking), and 3) the activation of weakening and

strengthening deformation mechanisms during individual slip events is associated with specific acoustic emissions.

2 Materials and Methods

We performed rotary shear experiments on simulated faults made of PMMA. The presented experimental configuration and dataset allow us to monitor seismic cycles in the laboratory.

2.1 The energy-controlled rotary shear machine (ECoR)

The energy-controlled rotary shear machine (ECoR, Rieger 2013) is a compact tabletop device (~ 0.5 m x 0.5 m x 1 m) that consists of a metal frame supporting a two-part central column (Figure 1). The lower column is fitted with a brushless motor that loads a clock spring (Figure 1b), which is connected to the bottom-rotating sample by an axle. The spring assembly increases the machine's compliance and, when loaded, applies a linearly increasing torque to the sample. We define the spring loading rate measured in MPa/s as $\dot{\tau}$. This configuration allows slip events to nucleate and arrest spontaneously along the simulated fault. While the dynamics of these events are partially influenced by the inertia of the rotating mechanical parts and the friction of the ball bearings, our machine response characterization suggests that the inertial effect is negligible within the scope of this work (Text S1). The rotary format allows displacements on the order of centimeters at typical seismic slip velocities (up to 1.5 m/s). In addition, experiments can be performed for nominally infinite duration, with several hundred to thousands of stick-slip events. Each event is analogous to an earthquake in nature - from the elastic loading (preseismic) to the post-seismic stress drop.

The upper column comprises the loading and sample assembly. The former is a vertical rod at the top of the column loaded with barbell plates. The weight of the plates is distributed over a plastic disc that transmits normal stress through four steel rods to the sample assembly. The rods are threaded through the frame via linear ball bearings so that the upper column can move vertically with minimum friction. The sample assembly comprises built-in sensors that measure the torque, normal stress, vertical displacement, and angular displacement of the sample and the motor (Figure

1c). Since the upper sample surface is annular, displacements in SI units are reported at the average sample radius as,

$$\boldsymbol{D} = \boldsymbol{\delta}\left(\frac{\boldsymbol{\pi}(\boldsymbol{R}+\boldsymbol{r})}{\mathbf{360}}\right), \qquad (\mathbf{1})$$

where D is displacement in meters, δ is the angular displacement, and R and r are the outer and inner radii in meters, respectively. We calculate shear stress from torque measurements (see Eq. 6 in Di Toro et al., 2010; Shimamoto and Tsutsumi, 1994). Mechanical signals are digitized and acquired with a National Instruments NI-4000 DAQ device. Data for all mechanical sensors are acquired at 35 kHz. We measure the interfacial temperature with two K-type thermocouples, one fed through the central axis of the upper sample and the other attached to its outer surface. These are acquired with Yocto-thermocouple^{TM} datalogger set to a sampling frequency between 25 and 100 Hz. This range corresponds to the length of the experiment as the data logger has limited storage capacity. To record and analyze the energy emitted as sound/ultrasonic waves, we use three acoustic emission (AE) sensors, two mounted on either side of the sample (sensors 1 and 2): a 5 mm diameter PZT-5A Boston piezoelectric transducer and a Glaser-type conical piezoelectric sensor (McLaskey & Glaser, 2010). A second 5 mm PZT-5A Boston piezoelectric transducer is mounted to the side of the machine frame (sensor 3). We transmit the AE signals through KRN AMP-1BB-AE preamplifiers to a PicoScope 4824A oscilloscope recording at a sampling rate of 2 MHz and a resolution of 12 bits. We used a transparent analog material (see section 2.2) to capture the evolution of the slip surface using a high-speed camera (Sony - DSC-RX100M5A) recording at 960 FPS.

2.2 Material: Polymethyl Methacrylate (PMMA) Glass

Samples were made of PMMA and worked into a hollow cylinder (15/2.5 mm external/internal radius; height 10–20 mm) installed in the upper column and a full cylinder (20 mm radius; height 10-20 mm) installed in the lower rotary column. The surface of the samples was prepared with a lathe and then polished for one minute with increasingly finer grit silicon carbide abrasive paper (600 grit – 1200 grit – 3000 grit – 3000 grit with water). We then cleaned the surface with alcohol to remove any dust and oils prior to the experiment. PMMA was selected because it has low hardness, low melting temperature, and is transparent, permitting direct observation of the slipping surface (see Table 1 for measured and referenced properties of PMMA). PMMA and other glasslike polymers have been extensively used in rupture mechanics studies (e.g., Ben-David et al., 2010; McLaskey & Glaser, 2011; McLaskey et al., 2012; Svetlizky & Fineberg, 2014). Indeed, the mechanical behavior of PMMA at standard temperature and pressure (STP) conditions closely resembles that of rocks in the Earth's crust (McLaskey et al., 2012; McLaskey & Glaser, 2011). This is due to the comparable homologous temperature (T_h = ambient temperature / melting temperature) between PMMA at STP conditions (T_{h_PMMA} = 293/418 in K = 0.7) and rocks with granitic compositions at seismogenic depths ($T_{h\_granite}$ = 0.7). Like in rocks, an increase in T_h determines the transition from an elasto-frictional to a visco-plastic regime in PMMA, as we demonstrate in the experiments presented here. Moreover, the melting of PMMA and its solidification into a glass changes its structure and induces more scattering as light passes through the material. Therefore, by illuminating the simulated fault with a laser beam, it is possible to distinguish solidified melt from undeformed PMMA. To investigate microstructures, we recovered samples from three experiments stopped during key phases of the experiment and imaged them with scanning electron microscopes (SEMs) JEOL JSM 6390 at 15 kV and JEOL JSM 6490 at 10 kV.

2.3 Energy flux calculations

Reches et al. (2019) argue that the energy flux (*EF*), or the rate of energy flow over the fault area, controls the slip style of natural fault systems. They suggest that slip continues until the frictional energy dissipation rate along the fault or power density ($PD = \tau V_{slip}$ with τ shear stress and V_{slip} slip rate, Di Toro et al., 2011) exceeds the *EF* to the fault. Therefore, we expect the interchange between the *EF* and *PD* to correlate with in-situ HFR video observations and AEs. We derive the *EF* from the spring by evaluating the spring potential energy,

$$PE_{spring} = \frac{1}{2}k\alpha^2 \tag{2}$$

with k the spring constant, and α the difference between the motor and sample rotation. To calculate the energy flux, we first find the power generated by the spring unloading (i.e., the time derivative of spring potential energy),

$$P_{spring} = \frac{dPE_{spring}}{dt} \tag{3}$$

EF_{spring} is:

$$EF_{spring} = -\frac{P_{spring}}{A}$$

Where A is the annular fault area. As a matter of sign convention, negative EF_{spring} indicates that the spring is loading (i.e., the stored energy is increasing), while positive

EF_{spring} indicates that the spring is unloading (i.e., providing energy to the fault). Since the fault surface is annular, V_{slip}, and $PD_{friction}$ are calculated at the average sample radius. Therefore, the $PD_{friction}$ estimate can be taken as an average for the slipping surface. We include spring and friction subscripts to clarify the corresponding energy source or sink, respectively.

3 Results

3.1. Mechanical data

We performed five experiments with the ECoR at constant normal stresses ranging from 3.4 to 3.7 MPa (Table 2). We performed three additional experiments (020620 and 102913) to produce fault slip zones to investigate with the SEM. These experiments (unlisted) yielded mechanical data very similar to those that investigate frictional melting using natural rocks (e.g., Del Gaudio et al., 2009 – Peridotite; Violay et al., 2014 – Gabbro, Violay et al., 2015 – Basalt; Cornelio et al., 2019 – Granite) by imposing, on the simulated faults, seismic slip rates on the order of 1 m/s. Additionally, the shear stress drops, $\Delta\tau$, produced by stick-slip events are comparable to natural earthquakes (e.g., Kobe 1995, magnitude = 7.2, $\Delta\tau \approx 2.4$ MPa, Allman and Shearer, 2009).

Each experiment started with a $\dot{\tau}$ of < 0.2 MPa/s, which resulted in low-frequency stick-slip events and a limited logarithmic increase (a few °C) of the sample temperature (Phase A). To raise the internal temperature of the sample and initiate melting during slip, $\dot{\tau}$ was raised to 1.1-2.5 MPa/s, increasing the frequency of stick-slip events. Following the $\dot{\tau}$ increase the stick slip behavior changed distinctly across three phases (phases B, C, and D, Figure 2).

Phase A. In this phase, we observe low amplitude stick-slip events with shear stress drops, < 0.7 MPa, occurring every 3.3–6.4 s (Figure 2). These events are associated with slip displacements of < 7 mm, average slip rates, V_{slip}, from 0.04 to 0.1 m/s, and peak slip rates, V_{peak}, from 0.1 to 0.2 m/s. The peak and residual friction, μ_p and μ_r, are 0.26–0.46 and 0.09–0.13, respectively, except for experiment 021622, where μ_r is an outlier at 0.33 (see discussion). The temperature increase during phase A in each experiment is < 5 °C. For all the reported phases V_{slip} and μ_r are calculated from the mechanical data (see Text S2) as the average value across the period where fault strength had stabilized after the friction drop (Figure 2, inset).

Phase B. Upon increasing the $\dot{\tau}$ to 1.1–2.5 MPa/s (varies between experiments), the period between stick-slip events decreases to 0.5–0.9 s, characterizing phase B (Figure 2). In phase B, stick-slip events have similar stress drops, residual friction, and velocities ($\Delta\tau < 0.8$ MPa, $\mu_r = 0.3$–0.5, $V_{\mathrm{peak}} = 0.1$–0.4 m/s and $V_{slip} = 0.03$–0.1 m/s, respectively). However, slip displacements are consistently higher (up to 7.8 mm) than in phase A (up to 7.0 mm). The sample temperature increases gradually up to roughly 40ºC. At this temperature, peak shear stress and the rate of temperature continues to climb (“runaway” in Figure 2), marking the transition to Phase C.

Phase C. This phase is characterized by $\tau_p > 3$ MPa, shear stress drops $\Delta\tau > 2.5$ MPa, μ_r between 0.25 and 0.46, and significant melt production and subsequent solidification and bonding (see section 4.3). Average stress drops are an order of magnitude higher than in phase B. V_{slip} and V_{peak} increase to 0.2–0.5 m/s and 0.6–1.0 m/s, respectively, and associated displacements exceed 2

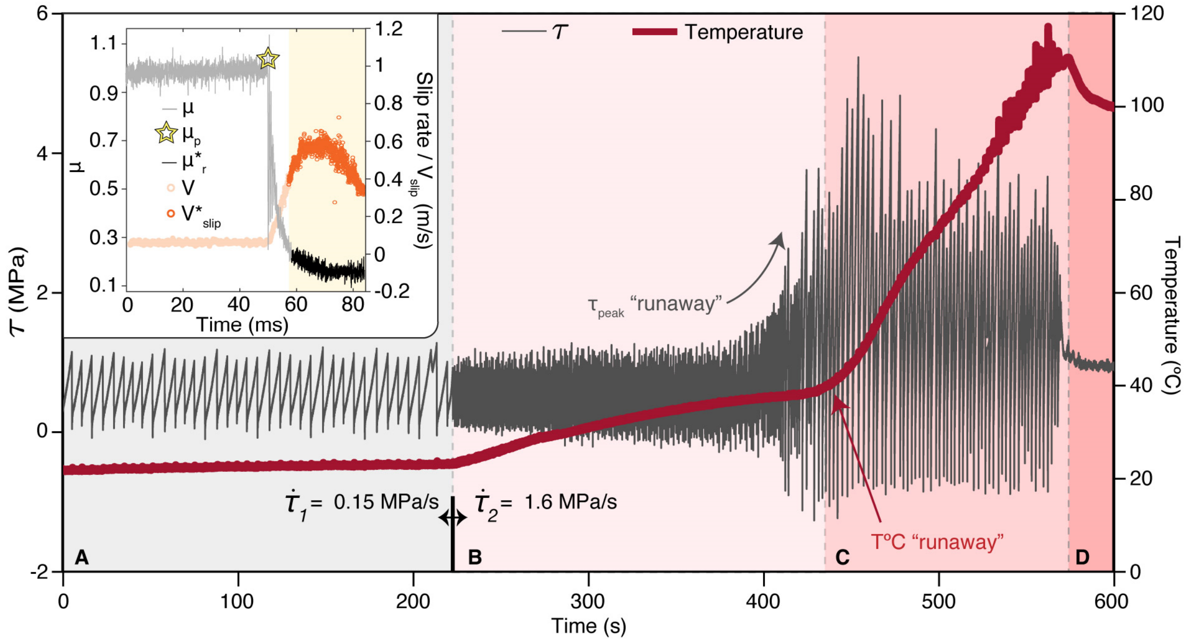

***Figure 2:** Evolution of shear stress and temperature with time in a typical experiment performed with ECoR (experiment 043021). **(a)** The spring loading rate (SRL) is increased after 220 s from 0.15 MPa/s to 1.6 MPa/s. Phase A is marked by low frequency but constant amplitude stick-slip events. Phase B begins once the SRL is increased to 1.6 MPa/s. At this higher SRL, the frequency of stick slip events and the rate of temperature rise increase. The increase in shear stress observed at the end of this phase corresponds to the start of significant melt production and fault strengthening. Phase C is marked by a sharp increase of the bulk temperature, peak shear stress, and stress drops. Eventually, the fault enters a stable sliding period, phase D, associated with the formation of a pervasive layer of melt. **(Inset)** Typical slip event (from phase C, experiment 021622) to show the quantities that variables in the text represent or are averaged over (marked with *). The approximate averaging window is shown in pale yellow.*

cm. Once fault temperature reaches ~110ºC, stable sliding begins, marking the initiation of Phase D (Figure 2).

Phase D. Upon entering phase D, there is a slight temperature decrease from 110°C to 100°C. This phase is characterized by continuous slip displacement, melt production and extrusion, and sample shortening. The residual shear stress μ_r stabilizes to 0.22–0.27, slightly higher than in phase C. Additionally, V_{slip} decreases to approximately 0.01 m/s. Three of the five experiments did not reach phase D because they were stopped before its onset (Table 2).

3.2 Energy flux and power densities

In Figure 3 a-d, we report the shear stress and EF_{spring} of typical slip events from phases A to D. The EF_{spring} curves have negative values in the pre-slip phase because of spring loading.

Phase A slip events have a maximum EF_{spring} of roughly 0.2 MW/m^2 (Figure 3a) and $PD_{friction}$ of 0.1–0.3 MW/m^2. Phase B events have maximum EF_{spring} values of 0.4 MW/m^2 (Figure 3b) while $PD_{friction}$ remains at 0.1-0.3 MW/m^2, with experiment 021622 as an outlier at $PD_{friction}$ = 0.6 MW/m^2. Phase C slip events have maximum EF_{spring} up to 3 MW/m^2 (Figure 3c). In phase C, an initial foreshock (stress drop and sharp AE signal marked with arrows in Figures. 3c and 3g) marks the onset of a continuous high-frequency signal (Figure 3g). Such AEs are possibly produced by microcracking and a precursory slow slip event of ~750 μm which is followed by the main fast slip event (i.e., laboratory earthquake). The $PD_{friction}$ during phase C ranges from 1 to 5.7 MW/m^2, much larger than in phases A and B.

3.3 Acoustic emissions

As all three-acoustic emission (AE) sensors recorded similar signals, we only report data from sensor 3 (Figure 3e-h). Typical phase A slip events exhibit small AE spikes up to ~1.8 V (Figure 3a, e). The amplitudes of AE signals from phase B events are similar to those of phase A but are followed by more pronounced harmonic oscillations (Figure 3f). In typical phase C slip

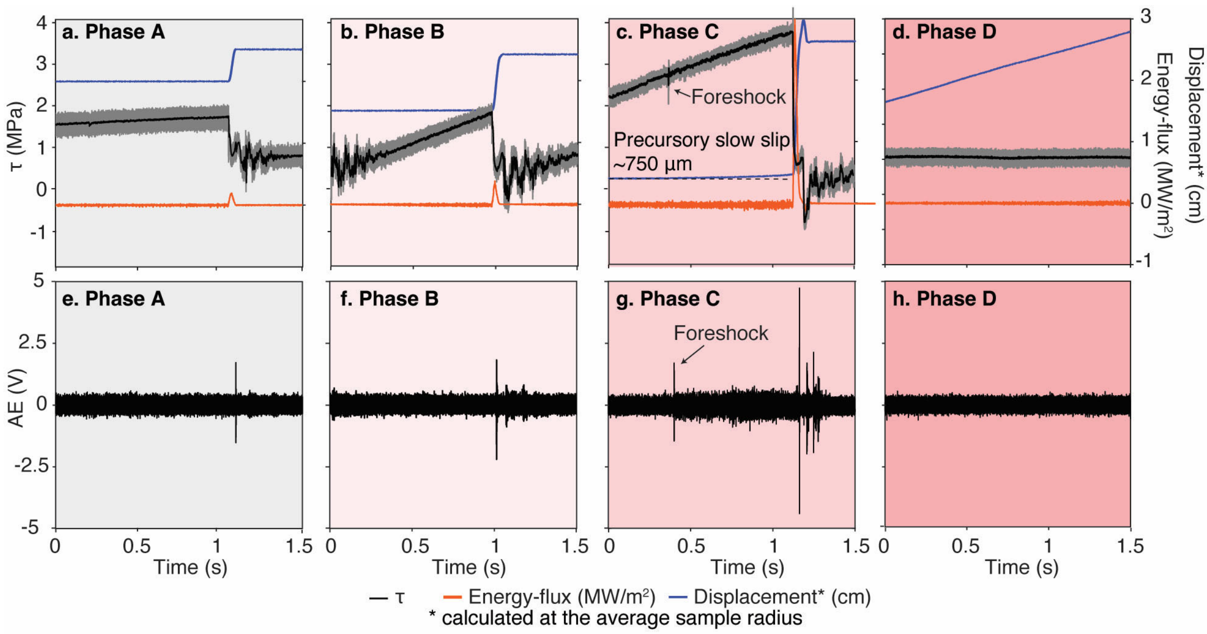

Figure 3: *Individual slip events within phases A-D of experiment 021622.* ***(a–d)*** *Plots of shear stress, displacement, and energy flux curves vs. time for single slip events from each phase.Since the sample is a hollow cylinder, the energy flux and displacement are calculated at the average sample radius (see section 2.1).* ***(e–h)*** *AEs accompanying events from each phase. Note the changes in precursory signals before the mainshock in phase C. The background colors correspond to those reported in figure 2. See text for discussion.*

events, we observe characteristic AE signals associated with precursory fault slow slip, fast slip, arrest, and slip reversal (Figure 3g, Figure 4). After a precursor AE (i.e., before section 1, time <31 ms in Figure 4), a low amplitude but continuous broadband (10-80 kHz) AE signal is associated with slow slip on the fault (~750 μm displacement before the event, Figure 3). This precursory phase is followed by an abrupt slip acceleration ("earthquake", section 1 in Figure 4), where the propagation of the fracture along the interface corresponds to a burst (0-20 dB/Hz) in power in the same frequency band, with a pronounced signal >20 dB/Hz between 14 and 45 kHz. The vibrations in the τ curve cease soon after the slip velocity overcomes ~0.2 m/s (section 2 in Figure 4). Notably, between ~5 ms and ~40 ms after the beginning of the earthquake, AEs have very low amplitude with few short, low-frequency spikes. Finally (section 3 in Figure 4), roughly 45 ms after the onset of unstable slip, a broadband burst up to 20 dB/Hz of AEs appears, which fades as the sample sliding stabilizes on a constant velocity until arrest. The AEs of phase D are relatively consistent and dominated by background noise (Figure 3h).

3.4 Fault in-situ observations

From the high frame rate recordings, we observe the microstructural evolution of the slipping zone throughout the experiments (Figure 5). The dark transparent color in Figure 5 is the relatively pristine slipping zone. The semi-opaque spots are melt patches and layers. Bright but transparent red features are interpreted as medium- to fine-grained PMMA or solidified melts. We support our interpretation of the images with sample investigations (section 3.4) at the corresponding phases. During phase A, small slip events are associated with an annular haze in the slipping zone, possibly due to the formation of an ultrafine gouge. Additionally, grooves become visible on the outer ring of the sample (Figure 5a, +10 ms after rupture). During phase B (Figure 5b), slip events produce additional gouge and discontinuous melt patches in the slipping

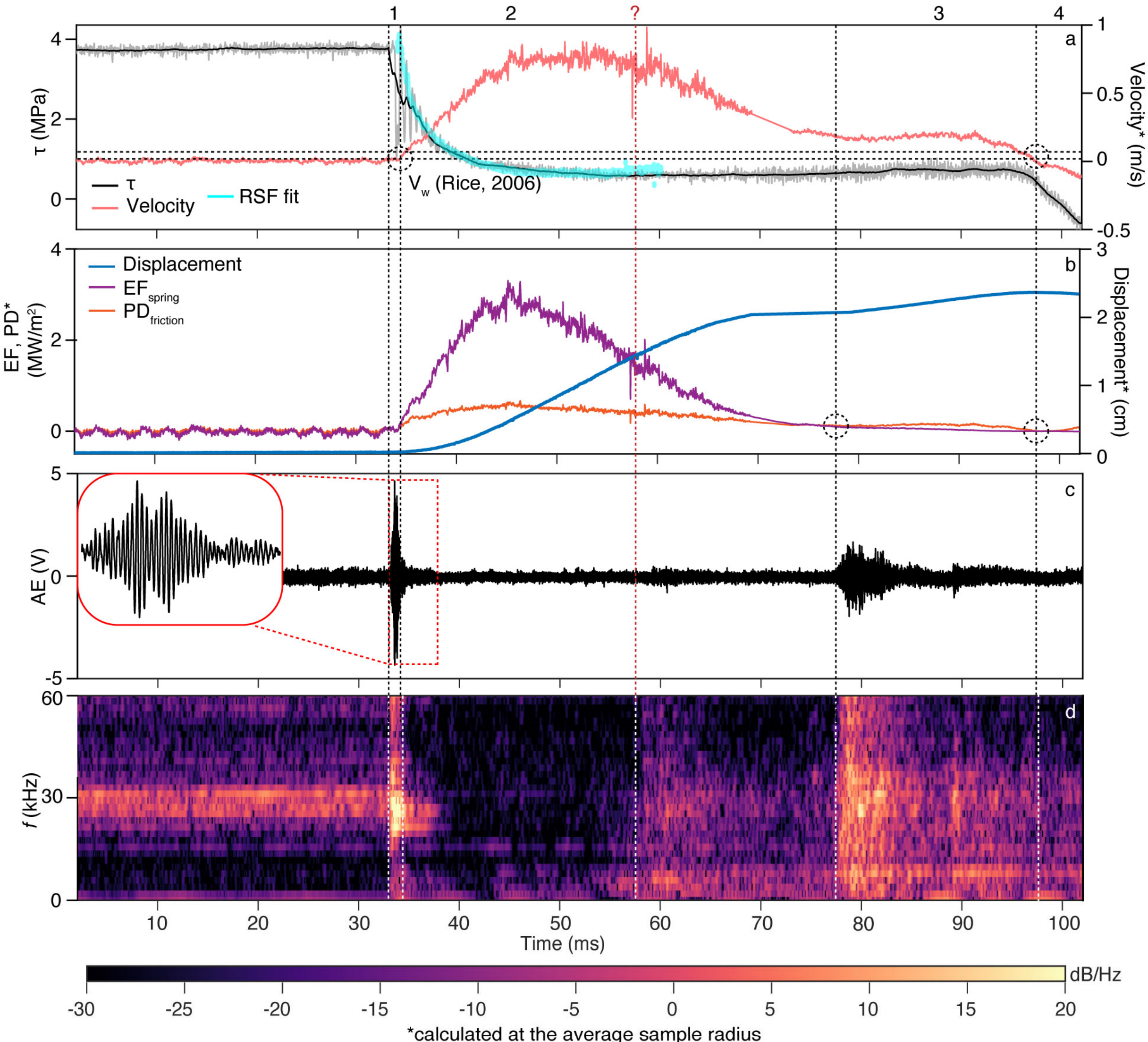

Figure 4: *Evolution of shear stress (τ), slip velocity (V), energy flux (EF), power density (PD) and acoustic emissions (AE) with time during a slip event of Phase C (experiment 021622).* ***(a)*** *The dependence of τ with time (black in color curve) is fit with the rate-and-state friction (RSF, cyan curve) also to determine* $D_{th} = 1 \times 10^{-5}$*m. The latter was fit iteratively with parameters: a = 0.04 and b = 0.25. The fault weakening velocity range,* V_w*, calculated after Rice (2006), is shown with horizontal dashed lines.* ***(b)*** *The spring energy flux (*EF_{spring}*), and the frictional power density (*$PD_{friction}$*) dissipated in this slip event.* ***(c)*** *AEs signal accompanying the slip event. The inset shows the wavelet corresponding to the initial shear stress drop.* ***(d)*** *Spectrogram of the AEs. Numbers on the top of the figure separated by vertical dashed lines indicate the style of cosesimic weakening/strengthening: (1) is the initial flash weakening stage across* D_{th}*, corresponding to a spike in the variance over frequency in the spectrogram; (2) is the melt lubrication stage which begins when the velocity crosses* V_w *and ends when the* EF_{spring} *and* PD_{curves} *curves intersect, marking the point where energy dissipated from friction exceeds that provided from the spring; (3) marks the activation of the viscous braking mechanism and ends when the velocity again crosses* V_w *and the interface is no longer in a weakened state; (4) marks the arrest and reversal of the sample due to the recoil of the assembly as it carries the rotational inertia of the event. The vertical red dotted line labeled with "?" marks the burst of AE power at ~58 ms, which corresponds to a characteristic break in the velocity time series.*

zone (+20 ms after rupture). With increasing slip and melt generation, a continuous melt ring forms, which welds the slipping zone once solidified (Figure 5c), marking the transition to phase C. During phase C, slip occurs when the welded interface breaks. Following this event (+5 ms after rupture), spots of melt and PMMA powders decorate the slipping zone. As slip ensues, the melt layer thickens and consumes the fine-grained PMMA (+20 ms after rupture). The darker transparent area in the outer ring is the unchanged surface between the upper and lower samples. Finally, in phase D (Figure 5d), a semi-opaque melt patch becomes visible up to 6 seconds after

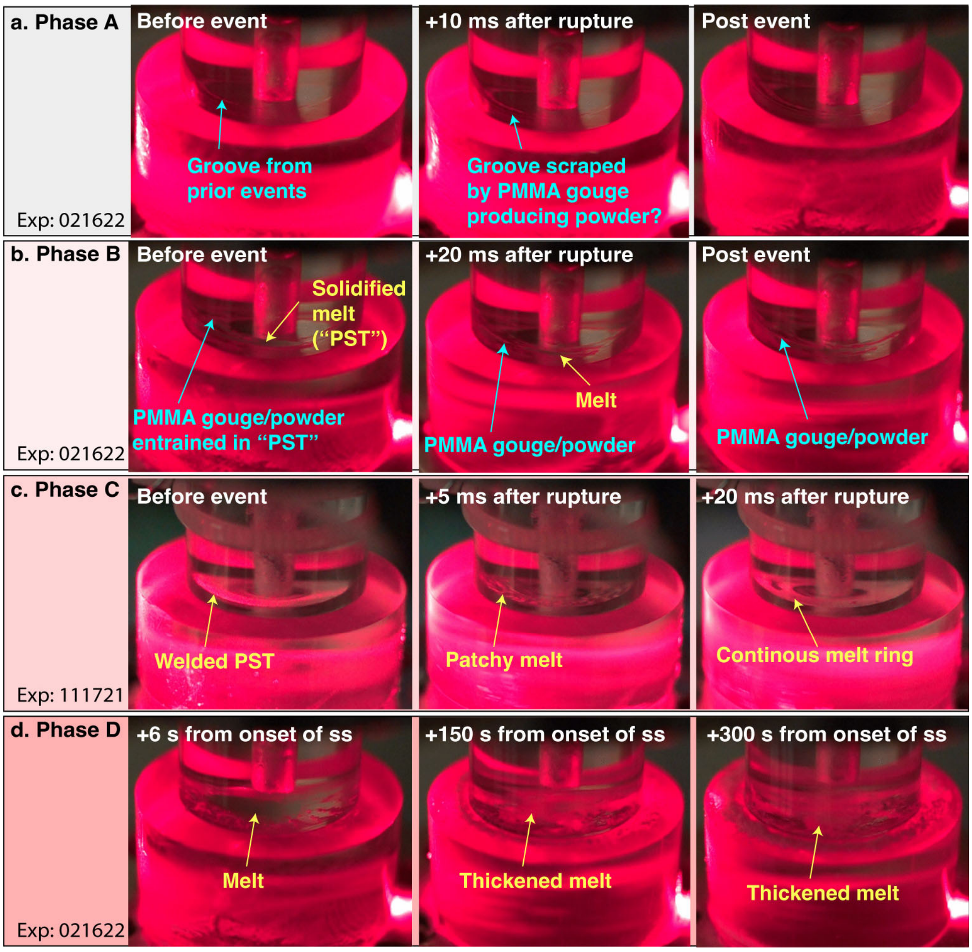

Figure 5: *Snapshots of high frame rate recordings during each phase of the experiment -experiment 021622 (a, b and d) and 111721 (c). The number of the experiment number is reported in the bottom left of the colored box. Blue and gold annotations represent solid and melt/pseudotachylyte (PST) features, respectively.* ***(a-c)*** *Three snapshots from individual events from phases A-C showing marked microstructural differences in their before, during and after slip event characteristics.* ***(d)*** *Changes occurring during Phase D with the continuation of stable sliding (ss). The background pinkish hues correspond to figures 2 and 4.*

the onset of stable sliding (ss). As stable sliding continues for >150 seconds, the melt patch becomes brighter and potentially thicker (thickened melt).

3.5 Microstructural observations

We investigated the microstructures of the experimental PMMA faults with scanning electron microscopes (Figure 6). The slip zone of the sample (recovered after phase C) is 5 to 14 μm thick (Figure 6a) and made of an aggregate of globular particles < 0.5 μm in size (Figure 6b). The contact between the slip zone and the lower sample is marked by a continuous < 0.2 μm thick film decorated with grooves and filaments sub-parallel to the slip vector (Figure 6b). Fractures with lengths < 118 μm and widths < 1 μm are visible in the upper sample (Figure 6a). We estimate the asperity widths on the lower sample to be ~10 μm (annotation in Figure 6a). To analyze the microstructural differences between low and high loading rate phases, we recovered the sample from an experiment stopped after phase A (Figure 6c) and an experiment stopped after phase C (Figure 6d). At the end of phase, A, the slip surface was decorated by fault steps and slickenlines. However, at the end of phase C, the slip surface is covered by clumps and a discontinuous layer of stretched filaments sub-parallel to the sliding direction. These glassy-like microstructures are similar to those found in experimental faults in silicate lithologies where frictional melting had occurred (Chen et al., 2017; Spray, 1995; Violay et al., 2014).

4. Discussion

Here we discuss the results of experiments performed with ECoR. This device is highly instrumented with torque, normal force, displacement, temperature, AEs sensors, and a high-frequency camera. The key benefit of the rotary approach is that experiments can be performed for "long" fault displacements producing data sets that allow us to study all phases of the earthquake cycle, including aseismic to seismic slip, fault healing, and stress loading (e.g., Reches and Lockner, 2010; Giacomel et al., 2018). Moreover, the torque loading spring in the ECoR adds the advantage that rupture nucleation, fault slip, and arrest emerge from complex feedbacks between the frequency of slip events and the strength, slip velocity, and temperature evolution of the fault zone. With the AE recordings, we discuss the appearance of characteristic signals associated with the various stages of seismic slip. Finally, we highlight the application of the results of these rock-analog experiments to natural conditions.

4.1 Interpretation of the mechanical data

Phases A-C are observed in all the experiments described here. However, phase D only occurs in the experiments with sufficient accumulated slip (Table 1). The transition from phase A to phases B-C-D is triggered by the increase in the spring loading rate from $\dot{\tau} < 0.2$ MPa/s to 1.1-2.5 MPa/s. Because of the short time interval between the slip events in phases B-C, frictional heat has less time to diffuse from the slip zone, and the ambient temperature increases (Figure 2). As a result, we observe marked differences between the dynamics of 1) small slip events, with no evidence of melting (phase A), 2) larger slip events possibly associated with discontinuous melt production (phase B), 3) large slip events associated with the formation of a continuous melt layer (Phase C), and 4) stable sliding at high ambient temperature and in the presence of melts (phase D, Figures 2, 5 and 6). This evolution in the frequency of slip events and fault strength with loading conditions demonstrates how the formation of frictional melts influences the seismic cycle and acts as both a lubricator and viscous brake during individual slip events (Kendrick & Lavallée, 2022).

Phase A. In this phase, we measure constant amplitude stick-slip events with μ_{peak} of 0.2–0.5 and dynamic weakening to μ_r of 0.1–0.3, similar to silicate rocks and industrial materials (Dieterich & Kilgore, 1994). The slight opacity of the slip surface and the presence of grooves (see Figure 5a) suggest that powders form from the grinding and plowing of asperities (Chen et al., 2017; Han et al., 2010, 2011; Reches & Lockner, 2010; Tisato et al., 2012). Microstructures are representative of brittle deformation processes, which include the formation of slickenlines and fault steps (e.g., Han et al., 2010, 2011; Siman-Tov et al., 2015) (Figure 6c). The presence of ultra-fine powders may contribute to fault weakening due to grain size and temperature-dependent deformation mechanisms in the successive phases (Green et al., 2015; Pozzi et al., 2021; Rowe et al., 2019; Spagnuolo et al., 2015). The anomalously high τ and μ values observed in phase A of experiment 021622 and, to a smaller extent, in phase B are attributed to differences in the initial fault surface roughness. Although we attempted to impose the same initial roughness by polishing the surfaces of all the samples with the same grit and for the same duration (see section 2.2), the deep groove formed during phases A-B of experiment 021622 suggests a large asperity or PMMA fragment is present in the slip zone which may increase τ (Figure 5a,b). However, with increasing slip distance, the spurious strength fades, possibly because of melting or plastic deformation of the asperity, and the data from phase C are consistent with those of the other experiments.

Phase B. This phase, where the frequency of stick-slip events increases and the ambient temperature rises from 25°C to 40°C, is transitional between phases A and C (Figure 2). Moreover, in phase B, heat diffusion from the slip zone reduces because the thermal diffusivity of PMMA decreases by roughly 10% as the temperature increases from 30 to 60 ºC (Assael et al., 2005). The higher frequency of slip events and the reduced thermal diffusivity of PMMA with increasing temperature may also explain why when the ambient temperature reaches approximately 40 ºC, the rate of temperature increase accelerates resulting in higher $\Delta\tau$, $\tau_{peak,}$ and τ_r typical of phase C. Chen et al. (2017) noted a similar transition in their experiments with granite, attributing the change in the mechanical behavior to the generation of "patchy melt along the fault". Out HFR recordings confirm their hypothesis as we observe the onset of melt patch generation (Figure 5c). While the measured bulk temperature (< 40 ºC) remains below the melting point of PMMA (130-160°C), the temperature at the asperity contacts (a few tens of μm in size at most) exceeds it (Rice 2006). We use a theoretical approach to estimate these "flash" temperatures because the spatial resolution and sampling rate of the thermocouple is too low to measure the temperature spike associated with individual slip events (Aretusini et al., 2021). For comparison, we include calculations for the "flash" temperature of phases A and C. The temperature spike at the asperities is (Rice, 2006):

$$\Delta T = \frac{\tau_c V t_{th}}{\rho c_p \sqrt{\pi \alpha_{th} t_{th}}}, \tag{4}$$

where τ_c is the stress concentrated at asperity tips, ρ density, α_{th} thermal diffusivity, and c_p heat capacity (see table 1 for PMMA). The t_{th} (= D_{th}/V_{slip}) is the sliding time duration at asperities of size D_{th}. We use a rate-and-state friction (RSF) law fit (Dieterich, 1972; Ruina, 1983) to estimate D_{th} (Figure 4a, blue curve) as 1×10^{-5} m, which approaches that estimated from SEM images of the slip surface (Figure 6) or reported in Dieterich & Kilgore (1994). The *a* and *b* RSF values were 0.04 and 0.25, respectively. This *b* value is higher than reported in the literature (0.0144, Kaneko et al., 2016). However, this discrepancy arises from the inversion of shear stress evolution with the RSF since the slip events in phase C are associated with melt formation (i.e., not “solid contacts” as in Kaneko et al., 2016). In addition, the initial velocity was higher due to precursory slow slip within this phase, which also increases the *b* value. In contrast, by using a phase A slip event with an initial velocity of $2x10^{-4}$ m/s (average velocity 100 ms before the event), we estimate the *b* value to be 0.03, much closer to that of Kaneko et al. (2016). We estimate τ_c, the stress concentrated at asperity tips as $\tau_c = 0.1*G$ (Boitnott et al., 1992; Dieterich & Kilgore, 1994, 1996), where *G* is the shear modulus of PMMA. Using the measured shear wave speed of PMMA, 1320 m/s, and ρ, 1.17–1.19 g/cm^3, we calculate *G* to be 2.08-2.04 GPa. Using the sliding velocity averaged across all experiments for V_{slip}, the ΔT at asperity tips for phases A-C are approximately 144-213ºC, 148-218ºC, and 311-459ºC, respectively.

The HFR images from phase B show the presence of solidified melt patches in the slip zone (Figure 5b). This observation is consistent with the estimated asperity scale temperatures discussed above and supports the hypothesis of rapid fault healing driven by local pseudotachylyte formation and fault welding (Mitchell et al., 2016; Proctor & Lockner, 2016; Hayward & Cox, 2017). Therefore, with successive slip events, because of fault strengthening, the EF_{spring} increases resulting in higher $PD_{friction}$ and more melt generation (positive feedback in phase B and especially in phase C). Eventually, as the cumulative effect of slip events provides more heat, the temperature increases, and the thermal runaway condition is achieved (transition to phase C, Figure 2).

Phase C. In this phase, the positive feedback established in phase B is more pronounced because of the high frequency of stick-slip events with large slip displacements, stress drops, and melt production. The ambient temperature increases from ∼50°C to ~105°C (Figure 2). During this temperature rise, additional melt is produced during each slip event leading to the formation of a thick and continuous melt layer (Figure 5c, Figure 6a,b). Correspondingly, the seismic slip dynamics in phase C are controlled by the increased presence of melt (see section 4.2).

Phase D. This phase starts when the ambient temperature overcomes the PMMA glass transition temperature of 105ºC (Figure 2), and molten PMMA no longer vitrifies and bonds the interface. The glass transition temperature marks the point where the rheology switches from elastoplastic to viscous-plastic, and the material relaxes at a rate higher than the strain rate and thus deforms viscously. Finally, stable sliding ensues when the melt forms a continuous and thick layer where viscous shear and heat retention exceed the heat dissipated, resulting in continuous sample consumption and melt production (Chen et al., 2017; Fialko & Khazan, 2005a; Nielsen et al., 2008). The result is a gradual strength stabilization as the molten layer is sheared (Fialko & Khazan, 2005a; Hirose & Shimamoto, 2005).

Similar phases to those described here have been observed in experimental studies on granite (Passelegue et al., 2016; Chen et al., 2017; Hung et al., 2019), gneiss (Hung et al., 2019), and gabbro (Hirose & Shimamoto, 2005; Niemejer et al., 2011). Chen et al. (2017) describe these phases as 1) initial weakening, 2) strengthening by viscous braking, 3) continuous melting of the fault surface, and 4) final strengthening due to melt freezing. Similarly, our A to D phases span Chen et al. phases 1-3, with an additional transitional phase between 1 and 2. We also add to their description static strengthening due to pseudotachylyte formation (Di Toro & Pennacchioni, 2005; Mitchell et al., 2016; Proctor & Lockner, 2016) and suggest that this may be a mechanism to assist in nucleating instabilities in the ductile realm. Our results highlight the complexity of the mechanical behavior of faults in the presence of frictional melts while demonstrating the similarities between PMMA and natural rocks.

4.2 Energy flux, power density, and acoustic emissions during coseismic fault slip

The dynamic mechanisms controlling the style and duration of sliding over the lifetime of a fault are not well constrained (Kanamori, 1994). For the strength of the slip interface to be perturbed, thermal processes must modify the material's elastic properties or reduce the effective normal stress (e.g., Brodsky & Kanamori, 2001; Kanamori & Heaton, 2000; Rice, 2006; Sibson, 1977; Violay et al., 2015). Fault friction generates heat which may cause rock melting (Sibson, 1977). While melting represents a sink of energy and may lead to lubrication and weakening (Sibson, 1975; Di Toro et al., 2011), cooling leads to relative viscous strengthening (Motohashi et al., 2019). And as discussed in section 5.1, glass formation may bond the opposing slip surfaces and strengthen the fault (Di Toro and Pennacchioni, 2005).

Kanamori and Heaton (2000) describe the effects of such thermal processes on the earthquake energy budget and show that they can strongly affect earthquake dynamics. Their hypothesis is supported by the observations of Kanamori (1994), that there is often a large discrepancy between the total potential energy released during faulting and the amount of radiated energy. The excess of non-radiated energy may be attributed to thermal, friction-related processes, typically comprising ~70% of the total energy budget. Kanamori's observation implies that thermally driven mechanisms such as flash melting, melt lubrication, and pseudotachylyte freezing may interact during faulting to control seismic slip. To understand the activation and interaction of these mechanisms, we derive and monitor the work rate. The latter describes the exchange of work provided by the release of stored elastic strain energy with dissipative physical or chemical processes within the slipping zone (Rice, 2006; Di Toro et al., 2011). In terms of the work done by the loading system, this quantity is the energy flux (Reches et al., 2019, Reches, 2020), whereas, in terms of the work done by frictional mechanisms, it is the power density (Rice, 2006; Di Toro et al., 2011; Reches, 2020). Power density plays a crucial role in many thermal fault mechanisms as it likely provides the most suitable estimate of the frictional heating rate (Reches, 2020). For example, Siman-Tov et al. (2013, 2015) and Aretusini et al. (2021) found an agreement between experimentally measured temperatures and those estimated with $PD_{friction}$ when investigating the formation of mirror surfaces in carbonate faults. However, the EF_{spring} to the fault limits the $PD_{friction}$ and controls the dynamic slip behavior (Reches et al., 2019).

Figure 4b shows the relations between the activation of coseismic weakening mechanisms, EF_{spring}, $PD_{friction}$, and AEs. When the shear stress overcomes the interfacial strength, fault rupture occurs, and unstable slip begins (Bowden et al., 1966), associated with a significant drop in friction. We attribute part of this drop to the weakening effect of high-stress concentration on asperity tips at the onset of rupture, termed flash weakening. When sustained for a sufficient duration, this mechanism can produce melt (e.g., Di Toro et al., 2006; Motohashi et al., 2019; Rice, 2006). When melting occurs, part of the energy is absorbed by the latent heat of fusion of the PMMA. Furthermore, once the average temperature of the surfaces is sufficiently high, the pressurization of melt may lubricate the fault by supporting the normal stress (Tullis, 2015 and references therein). Flash weakening occurs over a critical thermal slip distance, D_{th}, over which the sample moves at a velocity that exceeds the critical weakening velocity. We calculate the weakening velocity V_w as (Rice, 2006):

$$\boldsymbol{V_w = \frac{\pi\alpha_{th}}{D_{th}}\left(\frac{\rho c_p(T_w - T)}{\tau_c}\right)^2} \quad (5)$$

The weakening temperature, T_w, was taken to be the melting temperature, 130-160ºC (Smith & Hashemi, 2006), and T is the ambient room temperature measured to be 23ºC. From Eq. 11, V_w is 0.02–0.07 m/s, which is reported in Figure 4a with two dashed horizontal lines.

Flash weakening and the initiation of unstable slip across D_{th} (Figure 4, section 1) occur until the EF_{spring} and $PD_{friction}$ curves intersect (Figure 4a), and the velocity curve crosses V_w (Figure 4b). After this, τ_r begins to recover its quasi-static value of 0.6–0.8 MPa (see Table 2). Similar behavior has been recognized in experiments with a variety of rock types (e.g., Goldsby & Tullis, 2011). For this and other large events, the quasi-static value of τ corresponds to a residual friction, μ_r of 0.1–0.2, which is lower than the μ_r reported in the literature, typically ~0.4 (e.g., Lee & Golden, 1988; McCarthy et al., 2016). $PD_{friction}$ rapidly increases, corresponding to the more available EF_{spring} after the reduction of the interfacial strength and onset of high-velocity slip.

In Figure 4d, the sharp reduction in power apparent in the spectrogram after the mainshock may be explained by the "anelastic" effect of melt which would attenuate the AE signal (e.g., Karato & Spetzler, 1990; Ma et al., 2020). Furthermore, melt lubrication would effectively dampen the AE source by cushioning the interaction between asperities. When $PD_{friction}$ overcomes EF_{spring} (Figure 4, section 3), the amount of heat that can be generated by friction or viscous shearing is limited. We suggest this happens when the rate of heat diffusion exceeds that of heat production and melt begins to cool at a faster rate, increase in viscosity, and act as a braking mechanism, ultimately leading to the arrest of the sample (Fialko & Khazan, 2005b; Kendrick et al., 2014; Lavallée et al., 2012; Motohashi et al., 2019).

Considering the AEs, mechanical data, EF_{spring}, and $PD_{friction}$ discussed above, as a variation to what is posited by Reches et al. (2019), high-velocity slip is maintained when the energy flux to the fault equals or exceeds the power density. Yet, when overcome, the slip event enters a viscous braking phase rather than immediately coming to rest. In the AEs signal, a roughly 50 dB/Hz increase in power in the 0–100 kHz band seemingly corresponds to this phase (Figure 4c) which gradually fades impending arrest. These observations suggest that in addition to dehydration, fluid flow, and crack cascades (Burlini et al., 2009; Lockner, 1993), strengthening/weakening fault mechanisms activated in the experiments have peculiar AEs (Figure 4d), which may have their equivalent seismic signal in nature (Figure 4d). When the energy provided by the spring is entirely dissipated and the velocity again crosses V_w, the sample arrests and reverses direction as it carries the rotational inertia of the event (i.e., recoils, Figure 4, section 4). After final arrest, the interface drops below the glass transition temperature, and the melt solidifies into a pseudotachylyte and welds the fault. We provide additional examples from experiment 021622 of the *AEs* associated with the activation of strengthening/weakening mechanisms in Figure 7.

4.3 Application of the experimental observations to natural conditions

The experiments performed with the ECoR on PMMA support several field-based observations regarding faults decorated by pseudotachylytes hosted in silicate rocks. For instance, the experiments presented here support the occurrence of frictional melt lubrication associated with seismic slip in upper crustal faults (Sibson, 1975; Di Toro et al., 2006) (Figures 3b-c, 5b-c, and 6). Moreover, our results also indicate a static strengthening mechanism related to glass formation and fault welding, which may hinder fault reactivation by increasing fault post-slip strength (Di Toro & Pennacchioni, 2005; Mitchell et al., 2016; Proctor & Lockner, 2016).

Pseudotachylyte formation in nature may also occur in the lower crust and the upper mantle within the so-called ductile field (Jiang et al., 2015; Passchier et al., 1991; Pennacchioni & Cesare, 1997; Pittarello et al., 2012; Sibson, 1980; Ueda et al., 2008). In phase C, when the ambient temperature reaches ~50ºC, the homologous temperature of PMMA is 0.75. This homologous temperature corresponds to an ambient temperature in granite of ~600ºC, which is well within the ductile deformation field. Intermediate-depth earthquakes suggest that shear instabilities exist within this field (Hobbs et al., 1986; Karato et al., 2001; Kelemen & Hirth, 2007; Ogawa, 1987). One explanation for the nucleation of instabilities under such conditions is strain localization around a discontinuity in the deforming body. In this case, pseudotachylyte may provide small-

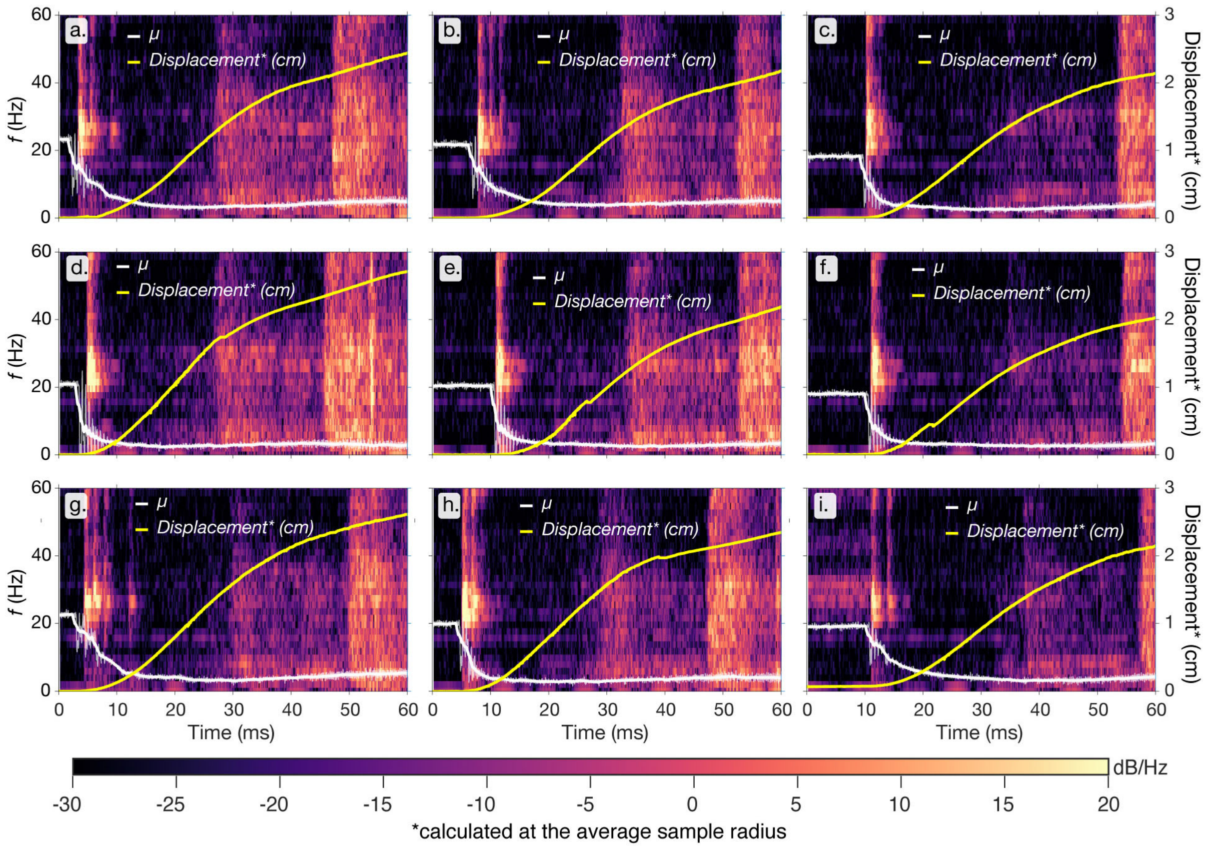

Figure 7: *Additional examples of acoustic emissions (AE) from Phase C events in experiment 021622. These results demonstrate the repeatability of the results presented in Figure 4.* ***(a-h)*** *Events without a foreshock. Therefore, they lack the 20 – 40 Hz signal apparent in Figure 4.* ***(i)*** *An example of an event with a foreshock similar to Figure 4 and thus a 20-40 Hz signal before rupture. See text for discussion.*

scale strength variations in a relatively homogenous body from which ductile instabilities can nucleate (Hobbs et al., 1986).

Finally, Kendrick et al. (2014) investigated the stick-slip ascent dynamics of magmatic plugs along boundary faults at ~400-600°C in the Saint Helens volcano. The authors reproduced fault slip through high-velocity rotary-shear experiments on andesite. They found that frictional melt dynamics (melt generation and lubrication, viscous breaking, and solidification) control slip instabilities and stick-slip cyclicity in these faults. The stick-slip events of phase C presented here support the role of friction melts and pseudotachylytes to assist in nucleating instabilities at such relatively high homologous temperatures (Figure 2).

5. Conclusions

We performed experiments on PMMA with a newly-conceived rotary shear machine (ECoR, Figure 1). The ECoR has proven to be a valid methodology for studying the evolving behavior of seismogenic faults across their lifetime, monitoring the activation of weakening/strengthening mechanisms, and capturing the earthquake nucleation and arrest processes. In particular, the mechanical data, temperature measurements, and high frame rate recordings suggest that the formation of frictional melts markedly impacts the simulated seismic cycle (Figures 2-3 5). The temperature rise on the slip zone, driven by the increased fault loading rate, facilitates melt production by providing the EF_{spring} needed for substantial frictional heating (Figures 2, 4). Melt formation controls individual slip events and, once the melt is solidified, the interseismic strengthening (i.e., pseudotachylyte formation and fault welding, Figures 2, 6). This positive feedback leads to a bulk temperature increase until a final phase of fault weakening in the presence of melts is achieved (Figure 2).

During individual slip events, flash heating and melting weaken the experimental faults (Rice, 2006). The EF_{spring} pulses provide the "fuel" for sustained sliding and continuous melt production and the transition to the frictional melt lubrication regime (Di Toro et al., 2006). However, once the $PD_{friction}$ overcomes the EF_{spring}, a viscous strengthening/braking regime is achieved, and fault slip is arrested. After the melt has cooled into a pseudotachylyte, it welds the slip surfaces (interseismic strengthening). This behavior allows stored elastic strain energy to be released in the subsequent slip event and may influence the localization of future fault activity (Di Toro & Pennacchioni, 2005; Mitchell et al., 2016; Proctor & Lockner, 2016). Interseismic strengthening also leads to larger slip events and, thus, higher V_{slip} and EF_{spring} and more melt production.

Since the homologous temperature of PMMA increases with the bulk fault temperature in phase B and especially phase C, the material is presumably in the viscous-plastic deformation regime (homologous temperature corresponding to ~600ºC in granite). Earthquakes in this realm may nucleate due to strain localization around a discontinuity in the deforming body, in which pseudotachylyte is a possible candidate (Hobbs et al., 1986) or by thermal runaway mechanisms in the slipping zone (Keleman and Hirth, 2007). Following these possibilities, in our experiments, the formation of pseudotachylytes and the increase of the bulk average temperature seem to have a pivotal role in generating the slip instabilities we observe in phase C (Figure 2-3). In support of this conclusion, we find that in phase D, stable sliding is initiated once the bulk fault temperature exceeds the glass transition temperature of PMMA. The relation between the deformation of frictional melt and the glass transition temperature is described by Kendrick & Lavallée (2022) and Lavallée et al. (2015).

Finally, we provide evidence that the activation of weakening/strengthening deformation mechanisms during simulated seismic slip manifests in acoustic signals (Figure 4c-d). While current seismic monitoring practices do not produce datasets with the resolution required to extract signals possibly related to fault strengthening and weakening, we propose that they are likely also present during natural events. With improved instrumentation close to the fault and enhanced analysis methods, they may be accessible and provide crucial information about the earthquake process.

Acknowledgments

We thank B. Cordonnier for assistance with early designs of the ECoR, experiments, and discussions. In addition, we thank B. Cordonnier and P. Orlandini for their technical assistance in providing SEM images and T.W. Becker, L. Lavier, and O. Almouidi for valuable discussions about the data. The manuscript was significantly improved thanks to reviews by the editor, Y. Bernabe, L. Yao and an anonymous reviewer.

Open research

The data associated with this work can be accessed via the Texas Data Repository (Conrad et al., 2022).

References

Aretusini, S., Meneghini, F., Spagnuolo, E., Harbord, C. W., & Di Toro, G. (2021). Fluid pressurisation and earthquake propagation in the Hikurangi subduction zone. Nature Communications, 12(1), 2481. https://doi.org/10.1038/s41467-021-22805-w

Assael, M. J., Botsios, S., Gialou, K., & Metaxa, I. N. (2005). Thermal Conductivity of Polymethyl Methacrylate (PMMA) and Borosilicate Crown Glass BK7. *International Journal of Thermophysics*, *26*(5), 1595–1605. https://doi.org/10.1007/s10765-005-8106-5

Badt, N. Z., Tullis, T. E., Hirth, G., & Goldsby, D. L. (2020). Thermal Pressurization Weakening in Laboratory Experiments. *Journal of Geophysical Research: Solid Earth*, *125*(5), e2019JB018872. https://doi.org/10.1029/2019JB018872

Barbery, M. R., Chester, F. M., & Chester, J. S. (2021). Characterizing the Distribution of Temperature and Normal Stress on Flash Heated Granite Surfaces at Seismic Slip Rates. *Journal of Geophysical Research: Solid Earth*, *126*(5), e2020JB021353. https://doi.org/10.1029/2020JB021353

Beeler, N. M., Tullis, T. E., & Goldsby, D. L. (2008). Constitutive relationships and physical basis of fault strength due to flash heating. *Journal of Geophysical Research: Solid Earth*, *113*(B1). https://doi.org/10.1029/2007JB004988

Ben-David, O., Rubinstein, S. M., & Fineberg, J. (2010). Slip-stick and the evolution of frictional strength. *Nature*, *463*(7277), 76–79. https://doi.org/10.1038/nature08676

Boitnott, G. N., Biegel, R. L., Scholz, C. H., Yoshioka, N., & Wang, W. (1992). Micromechanics of rock friction 2: Quantitative modeling of initial friction with contact theory. *Journal of Geophysical Research: Solid Earth*, *97*(B6), 8965–8978. https://doi.org/10.1029/92JB00019

Bowden, F. P., & Tabor, D. (1954). The friction and lubrication of solids. New York: Oxford University Press.

Brodsky, E. E., & Kanamori, H. (2001). Elastohydrodynamic lubrication of faults. *Journal of Geophysical Research: Solid Earth*, *106*(B8), 16357–16374. https://doi.org/10.1029/2001JB000430

Burlini, L., Di Toro, G., & Meredith, P. (2009). Seismic tremor in subduction zones: Rock physics evidence. *Geophysical Research Letters*, *36*(8). https://doi.org/10.1029/2009GL037735

Chen, X., Elwood Madden, A. S., & Reches, Z. (2017). Friction Evolution of Granitic Faults: Heating Controlled Transition From Powder Lubrication to Frictional Melt. *Journal of Geophysical Research: Solid Earth*, *122*(11), 9275–9289. https://doi.org/10.1002/2017JB014462

Chen, X., Madden, A. S. E., & Reches, Z. (2017). Powder Rolling as a Mechanism of Dynamic Fault Weakening. In *Fault Zone Dynamic Processes* (pp. 133–150). American Geophysical Union (AGU). https://doi.org/10.1002/9781119156895.ch7

Conrad, E. M., Tisato, N., Carpenter, B. M., Di Toro, G. (2022). Data for: "Influence of Frictional Melt on the Seismic Cycle: Insights from Experiments on Rock Analog Material". Texas Data Repository Dataverse. https://doi.org/10.18738/T8/6JOR2D

De Paola, N., Hirose, T., Mitchell, T., Di Toro, G., Viti, C., & Shimamoto, T. (2011). Fault lubrication and earthquake propagation in thermally unstable rocks. Geology, 39(1), 35–38. https://doi.org/10.1130/G31398.1

Del Gaudio, P., Di Toro, G., Han, R., Hirose, T., Nielsen, S., Shimamoto, T., & Cavallo, A. (2009). Frictional melting of peridotite and seismic slip. *Journal of Geophysical Research: Solid Earth*, *114*(B6). https://doi.org/10.1029/2008JB005990

Di Toro, G., Han, R., Hirose, T., De Paola, N., Nielsen, S., Mizoguchi, K., et al. (2011). Fault lubrication during earthquakes. *Nature*, *471*(7339), 494–498. https://doi.org/10.1038/nature09838

Di Toro, G., & Pennacchioni, G. (2005). Fault plane processes and mesoscopic structure of a strong-type seismogenic fault in tonalites (Adamello batholith, Southern Alps). *Tectonophysics*, *402*(1–4), 55–80. https://doi.org/10.1016/j.tecto.2004.12.036

Di Toro, G., Hirose, T., Nielsen, S., & Shimamoto, T. (2006). Relating high-velocity rock-friction experiments to coseismic slip in the presence of melts. In R. Abercrombie, A. McGarr, H. Kanamori, & G. Di Toro (Eds.), *Geophysical Monograph Series* (Vol. 170, pp. 121–134). Washington, D. C.: American Geophysical Union. https://doi.org/10.1029/170GM13

Dieterich, J. H. (1978). Preseismic fault slip and earthquake prediction. *Journal of Geophysical Research: Solid Earth*, *83*(B8), 3940–3948. https://doi.org/10.1029/JB083iB08p03940

Dieterich, J.H. (1972). Time-dependent friction in rocks. *Journal of Geophysical Research (1896-1977)*, *77*(20), 3690–3697. https://doi.org/10.1029/JB077i020p03690

Dieterich, J.H. (1979). Modeling of rock friction: 1. Experimental results and constitutive equations. *Journal of Geophysical Research: Solid Earth*, *84*(B5), 2161–2168. https://doi.org/10.1029/JB084iB05p02161

Dieterich, J.H., & Kilgore, B. D. (1994). Direct observation of frictional contacts: New insights for state-dependent properties. *Pure and Applied Geophysics*, *143*(1), 283–302. https://doi.org/10.1007/BF00874332

Dieterich, J.H., & Kilgore, B. D. (1996). Imaging surface contacts: power law contact distributions and contact stresses in quartz, calcite, glass and acrylic plastic. *Tectonophysics*, *256*(1–4), 219–239. https://doi.org/10.1016/0040-1951(95)00165-4

Faulkner, D. R., Sanchez-Roa, C., Boulton, C., & den Hartog, S. a. M. (2018). Pore Fluid Pressure Development in Compacting Fault Gouge in Theory, Experiments, and Nature. Journal of Geophysical Research: Solid Earth, 123(1), 226–241. https://doi.org/10.1002/2017JB015130

Fialko, Y., & Khazan, Y. (2005a). Fusion by earthquake fault friction: Stick or slip? *Journal of Geophysical Research: Solid Earth*, *110*(B12). https://doi.org/10.1029/2005JB003869

Fialko, Y., & Khazan, Y. (2005b). Fusion by earthquake fault friction: Stick or slip? *Journal of Geophysical Research: Solid Earth*, *110*(B12). https://doi.org/10.1029/2005JB003869

Giacomel, P., Spagnuolo, E., Nazzari, M., Marzoli, A., Passelegue, F., Youbi, N., & Di Toro, G. (2018). Frictional Instabilities and Carbonation of Basalts Triggered by Injection of Pressurized H2O- and CO2- Rich Fluids. *Geophysical Research Letters*, *45*(12), 6032–6041. https://doi.org/10.1029/2018GL078082

Goldsby, D. L., & Tullis, T. E. (2011). Flash Heating Leads to Low Frictional Strength of Crustal Rocks at Earthquake Slip Rates. *Science*, *334*(6053), 216–218. https://doi.org/10.1126/science.1207902

Green II, H. W., Shi, F., Bozhilov, K., Xia, G., & Reches, Z. (2015). Phase transformation and nanometric flow cause extreme weakening during fault slip. *Nature Geoscience*, *8*(6), 484–489. https://doi.org/10.1038/ngeo2436

Han, R., Hirose, T., & Shimamoto, T. (2010). Strong velocity weakening and powder lubrication of simulated carbonate faults at seismic slip rates. *Journal of Geophysical Research: Solid Earth*, *115*(B3). https://doi.org/10.1029/2008JB006136

Han, R., Hirose, T., Shimamoto, T., Lee, Y., & Ando, J. (2011). Granular nanoparticles lubricate faults during seismic slip. *Geology*, *39*, 599–602. https://doi.org/10.1130/G31842.1

Hayward, K. S., & Cox, S. F. (2017). Melt Welding and Its Role in Fault Reactivation and Localization of Fracture Damage in Seismically Active Faults. *Journal of Geophysical Research: Solid Earth*, *122*(12), 9689–9713. https://doi.org/10.1002/2017JB014903

Hirose, T., & Shimamoto, T. (2005). Growth of molten zone as a mechanism of slip weakening of simulated faults in gabbro during frictional melting. *Journal of Geophysical Research: Solid Earth*, *110*(B5). https://doi.org/10.1029/2004JB003207

Hobbs, B. E., Ord, A., & Teyssier, C. (1986). Earthquakes in the ductile regime? *Pure and Applied Geophysics*, *124*(1), 309–336. https://doi.org/10.1007/BF00875730

Hung, C.-C., Kuo, L.-W., Spagnuolo, E., Wang, C.-C., Di Toro, G., Wu, W.-J., et al. (2019). Grain Fragmentation and Frictional Melting During Initial Experimental Deformation and Implications for Seismic Slip at Shallow Depths. *Journal of Geophysical Research: Solid Earth*, *124*(11), 11150–11169. https://doi.org/10.1029/2019JB017905

Jiang, H., Lee, C.-T. A., Morgan, J. K., & Ross, C. H. (2015). Geochemistry and thermodynamics of an earthquake: A case study of pseudotachylites within mylonitic granitoid. *Earth and Planetary Science Letters*, *430*, 235–248. https://doi.org/10.1016/j.epsl.2015.08.027

Kanamori, H. (1994). Mechanics of earthquakes. *Annual Review of Earth and Planetary Sciences*, *22*(1), 207–237. https://doi.org/10.1146/annurev.ea.22.050194.001231

Kanamori, H., & Brodsky, E. E. (2004). The physics of earthquakes. *Reports on Progress in Physics*, *67*(8), 1429–1496. https://doi.org/10.1088/0034-4885/67/8/R03

Kanamori, H., & Heaton, T. H. (2000). Microscopic and macroscopic physics of earthquakes. In J. B. Rundle, D. L. Turcotte, & W. Klein (Eds.), *Geophysical Monograph Series* (Vol. 120, pp. 147–163). Washington, D. C.: American Geophysical Union. https://doi.org/10.1029/GM120p0147

Kaneko, Y., Nielsen, S. B., & Carpenter, B. M. (2016). The onset of laboratory earthquakes explained by nucleating rupture on a rate-and-state fault. *Journal of Geophysical Research: Solid Earth*, *121*(8), 6071–6091. https://doi.org/10.1002/2016JB013143

Karato, S., & Spetzler, H. A. (1990). Defect microdynamics in minerals and solid-state mechanisms of seismic wave attenuation and velocity dispersion in the mantle. *Reviews of Geophysics*, *28*(4), 399–421. https://doi.org/10.1029/RG028i004p00399

Karato, S., Riedel, M. R., & Yuen, D. A. (2001). Rheological structure and deformation of subducted slabs in the mantle transition zone: implications for mantle circulation and deep earthquakes. *Physics of the Earth and Planetary Interiors*, *127*(1–4), 83–108. https://doi.org/10.1016/S0031-9201(01)00223-0

Kelemen, P. B., & Hirth, G. (2007). A periodic shear-heating mechanism for intermediate-depth earthquakes in the mantle. *Nature*, *446*(7137), 787–790. https://doi.org/10.1038/nature05717

Kendrick, J. E., Lavallée, Y., Hirose, T., Di Toro, G., Hornby, A. J., De Angelis, S., & Dingwell, D. B. (2014). Volcanic drumbeat seismicity caused by stick-slip motion and magmatic frictional melting. *Nature Geoscience*, *7*(6), 438–442. https://doi.org/10.1038/ngeo2146

Kendrick, Jackie E., & Lavallée, Y. (2022). Frictional Melting in Magma and Lava. *Reviews in Mineralogy and Geochemistry*, *87*(1), 919–963. https://doi.org/10.2138/rmg.2022.87.20

Lavallée, Y., Mitchell, T. M., Heap, M. J., Vasseur, J., Hess, K.-U., Hirose, T., & Dingwell, D. B. (2012). Experimental generation of volcanic pseudotachylytes: Constraining rheology. *Journal of Structural Geology*, *38*, 222–233. https://doi.org/10.1016/j.jsg.2012.02.001

Lavallée, Y., Hirose, T., Kendrick, J. E., Hess, K.-U., & Dingwell, D. B. (2015). Fault rheology beyond frictional melting. *Proceedings of the National Academy of Sciences*, *112*(30), 9276–9280. https://doi.org/10.1073/pnas.1413608112

Lee, M. C. H., & Golden, M. A. (1988). The Coefficient of Friction of a Polyamide/Polymethyl Methacrylate Blend System. *Journal of Elastomers & Plastics*, *20*(2), 163–186. https://doi.org/10.1177/009524438802000207

Lin, A. (2007). *Fossil Earthquakes: The Formation and Preservation of Pseudotachylytes*. Springer.

Lockner, D. (1993). The role of acoustic emission in the study of rock fracture. *International Journal of Rock Mechanics and Mining Sciences & Geomechanics Abstracts*, *30*(7), 883–899. https://doi.org/10.1016/0148-9062(93)90041-B

Lockner, D. A., Kilgore, B. D., Beeler, N. M., & Moore, D. E. (2017). The Transition From Frictional Sliding to Shear Melting in Laboratory Stick-Slip Experiments. In M. Y.

Thomas, T. M. Mitchell, & H. S. Bhat (Eds.), *Geophysical Monograph Series* (pp. 103–131). Hoboken, NJ, USA: John Wiley & Sons, Inc. https://doi.org/10.1002/9781119156895.ch6

Ma, M., Zhang, J., Zhou, X., & Xu, Z. (2020). The melt content of the low velocity layer atop the mantle transition zone: Theory and method of calculation. *MethodsX*, *7*, 100751. https://doi.org/10.1016/j.mex.2019.11.024

Marone, C. (1998). LABORATORY-DERIVED FRICTION LAWS AND THEIR APPLICATION TO SEISMIC FAULTING. *Annual Review of Earth and Planetary Sciences*, *26*(1), 643–696. https://doi.org/10.1146/annurev.earth.26.1.643

McCarthy, C., Savage, H. M., Koczynski, T., & Nielson, M. A. (2016). An apparatus to measure frictional, anelastic, and viscous behavior in ice at temperate and planetary conditions. *Review of Scientific Instruments*, *87*(5), 055112. https://doi.org/10.1063/1.4950782

McLaskey, G. C., & Glaser, S. D. (2010). Hertzian impact: Experimental study of the force pulse and resulting stress waves. *The Journal of the Acoustical Society of America*, *128*(3), 1087–1096. https://doi.org/10.1121/1.3466847

McLaskey, G. C., & Glaser, S. D. (2011). Micromechanics of asperity rupture during laboratory stick slip experiments: ASPERITY RUPTURE MICROMECHANICS. *Geophysical Research Letters*, *38*(12), n/a-n/a. https://doi.org/10.1029/2011GL047507

McLaskey, G. C., Thomas, A. M., Glaser, S. D., & Nadeau, R. M. (2012). Fault healing promotes high-frequency earthquakes in laboratory experiments and on natural faults. *Nature*, *491*(7422), 101–104. https://doi.org/10.1038/nature11512

Mitchell, T. M., Toy, V., Di Toro, G., Renner, J., & Sibson, R. H. (2016). Fault welding by pseudotachylyte formation. *Geology*, *44*(12), 1059–1062. https://doi.org/10.1130/G38373.1

Motohashi, G., Oohashi, K., & Ujiie, K. (2019). Viscous strengthening followed by slip weakening during frictional melting of chert. *Earth, Planets and Space*, *71*(1), 55. https://doi.org/10.1186/s40623-019-1035-5

Newman, J., Lamb, W. M., Drury, M. R., & Vissers, R. L. M. (1999). Deformation processes in a peridotite shear zone: reaction-softening by an H2O-deficient, continuous net transfer reaction. *Tectonophysics*, *303*(1), 193–222. https://doi.org/10.1016/S0040-1951(98)00259-5

Nielsen, S., Di Toro, G., Hirose, T., & Shimamoto, T. (2008). Frictional melt and seismic slip. *Journal of Geophysical Research: Solid Earth*, *113*(B1). https://doi.org/10.1029/2007JB005122

Nielsen, S., Mosca, P., Giberti, G., Di Toro, G., Hirose, T., & Shimamoto, T. (2010). On the transient behavior of frictional melt during seismic slip. *Journal of Geophysical Research: Solid Earth*, *115*(B10). https://doi.org/10.1029/2009JB007020

Niemeijer, A., Di Toro, G., Griffith, W. A., Bistacchi, A., Smith, S. A. F., & Nielsen, S. (2012). Inferring earthquake physics and chemistry using an integrated field and laboratory approach. *Journal of Structural Geology*, *39*, 2–36. https://doi.org/10.1016/j.jsg.2012.02.018

Ogawa, M. (1987). Shear instability in a viscoelastic material as the cause of deep focus earthquakes. *Journal of Geophysical Research: Solid Earth*, *92*(B13), 13801–13810. https://doi.org/10.1029/JB092iB13p13801

Passchier, C. W., Bekendam, R. F., Hoek, J. D., Dirks, P. G. H. M., & Boorder, H. de. (1991). Proterozoic geological evolution of the northern Vestfold Hills, Antarctica. *Geological Magazine*, *128*(4), 307–318. https://doi.org/10.1017/S0016756800017581

Passelègue, F. X., Spagnuolo, E., Violay, M., Nielsen, S., Di Toro, G., & Schubnel, A. (2016). Frictional evolution, acoustic emissions activity, and off-fault damage in simulated faults sheared at seismic slip rates. *Journal of Geophysical Research: Solid Earth*, *121*(10), 7490–7513. https://doi.org/10.1002/2016JB012988

Peacock, S. M. (2001). Are the lower planes of double seismic zones caused by serpentine dehydration in subducting oceanic mantle? *Geology*, *29*(4), 299. https://doi.org/10.1130/0091-7613(2001)029<0299:ATLPOD>2.0.CO;2

Pennacchioni, G., & Cesare, B. (1997). Ductile-brittle transition in pre-Alpine amphibolite facies mylonites during evolution from water-present to water-deficient conditions (Mont Mary nappe, Italian Western Alps). *Journal of Metamorphic Geology*, *15*(6), 777–791. https://doi.org/10.1111/j.1525-1314.1997.00055.x

Pittarello, L., Pennacchioni, G., & Di Toro, G. (2012). Amphibolite-facies pseudotachylytes in Premosello metagabbro and felsic mylonites (Ivrea Zone, Italy). *Tectonophysics*, *580*, 43–57. https://doi.org/10.1016/j.tecto.2012.08.001

Pozzi, G., De Paola, N., Nielsen, S. B., Holdsworth, R. E., Tesei, T., Thieme, M., & Demouchy, S. (2021). Coseismic fault lubrication by viscous deformation. *Nature Geoscience*, *14*(6), 437–442. https://doi.org/10.1038/s41561-021-00747-8

Proctor, B., & Lockner, D. A. (2016). Pseudotachylyte increases the post-slip strength of faults. *Geology*, *44*(12), 1003–1006. https://doi.org/10.1130/G38349.1

Reches, Z. (2020). Dynamic Frictional Slip Along Rock Faults. *Journal of Tribology*, *142*(12). https://doi.org/10.1115/1.4047547

Reches, Z., & Lockner, D. A. (2010). Fault weakening and earthquake instability by powder lubrication. *Nature*, *467*(7314), 452–455. https://doi.org/10.1038/nature09348

Reches, Z., Zu, X., & Carpenter, B. M. (2019). Energy-flux control of the steady-state, creep, and dynamic slip modes of faults. *Scientific Reports*, *9*(1), 10627. https://doi.org/10.1038/s41598-019-46922-1

Rice, J. R. (2006). Heating and weakening of faults during earthquake slip. *Journal of Geophysical Research: Solid Earth*, *111*(B5). https://doi.org/10.1029/2005JB004006

Rieger, K., Cordonnier, B., Tisato, N., & Burg, J.-P. (2013, August). *From Brittle to Creep: Investigation of Fault Weakening Tribology Under Constant Loading Rate* (Master's). ETH Zürich, Zürich.

Roig Silva, C., Goldsby, D. L., di Toro, G., & Tullis, T. E. (2004). The Role of Silica Content in Dynamic Fault Weakening Due to Gel Lubrication, *2004*, T21D-06. Presented at the AGU Fall Meeting Abstracts.

Rowe, C. D., Lamothe, K., Rempe, M., Andrews, M., Mitchell, T. M., Di Toro, G., et al. (2019). Earthquake lubrication and healing explained by amorphous nanosilica. *Nature Communications*, *10*(1), 320. https://doi.org/10.1038/s41467-018-08238-y

Ruina, A. (1983). Slip instability and state variable friction laws. *Journal of Geophysical Research: Solid Earth*, *88*(B12), 10359–10370. https://doi.org/10.1029/JB088iB12p10359

Scambelluri, M., Pennacchioni, G., Gilio, M., Bestmann, M., Plümper, O., & Nestola, F. (2017). Fossil intermediate-depth earthquakes in subducting slabs linked to differential stress release. Nature Geoscience, 10(12), 960–966. https://doi.org/10.1038/s41561-017-0010-7

Shimamoto T., & Tsutsumi, A. (1994). A new rotary-shear high-speed frictional testing machine: its basic design and scope of research. *J Tecton Res Group Jpn* 39:65–78 (in Japanese with English abstract)

Sibson, R. H. (1977). Fault rocks and fault mechanisms. *Journal of the Geological Society*, *133*(3), 191–213. https://doi.org/10.1144/gsjgs.133.3.0191

Sibson, R. H. (1980). Transient discontinuities in ductile shear zones. *Journal of Structural Geology*, *2*(1), 165–171. https://doi.org/10.1016/0191-8141(80)90047-4

Sibson, R. H. (1975). Generation of Pseudotachylyte by Ancient Seismic Faulting. *Geophysical Journal International*, *43*(3), 775–794. https://doi.org/10.1111/j.1365-246X.1975.tb06195.x

Siman-Tov, S., Aharonov, E., Sagy, A., & Emmanuel, S. (2013). Nanograins form carbonate fault mirrors. *Geology*, *41*(6), 703–706. https://doi.org/10.1130/G34087.1

Siman-Tov, S., Aharonov, E., Boneh, Y., & Reches, Z. (2015). Fault mirrors along carbonate faults: Formation and destruction during shear experiments. *Earth and Planetary Science Letters*, *430*, 367–376. https://doi.org/10.1016/j.epsl.2015.08.031

Smith, W. F., & Hashemi, J. (2006). *Fundamentos de la ciencia e ingeniería de materiales (4a. ed.)*. México, D.F., MEXICO: McGraw-Hill Interamericana. Retrieved from http://ebookcentral.proquest.com/lib/utxa/detail.action?docID=3217207

Spagnuolo, E., Plümper, O., Violay, M., Cavallo, A., & Di Toro, G. (2015). Fast-moving dislocations trigger flash weakening in carbonate-bearing faults during earthquakes. *Scientific Reports*, *5*(1), 16112. https://doi.org/10.1038/srep16112

Spray, J. G. (1995). Pseudotachylyte controversy: Fact or friction? *Geology*, *23*(12), 1119. https://doi.org/10.1130/0091-7613(1995)023<1119:PCFOF>2.3.CO;2

Spray, J. G. (2005). Evidence for melt lubrication during large earthquakes. *Geophysical Research Letters*, *32*(7). https://doi.org/10.1029/2004GL022293

Spray, J. G. (2010). Frictional Melting Processes in Planetary Materials: From Hypervelocity Impact to Earthquakes. *Annual Review of Earth and Planetary Sciences*, *38*(1), 221–254. https://doi.org/10.1146/annurev.earth.031208.100045

Svetlizky, I., & Fineberg, J. (2014). Classical shear cracks drive the onset of dry frictional motion. *Nature*, *509*(7499), 205–208. https://doi.org/10.1038/nature13202

Tisato, N., Di Toro, G., De Rossi, N., Quaresimin, M., & Candela, T. (2012). Experimental investigation of flash weakening in limestone. *Journal of Structural Geology*, *38*, 183–199. https://doi.org/10.1016/j.jsg.2011.11.017

Tullis, T. E. (2015). Mechanisms for Friction of Rock at Earthquake Slip Rates. In *Treatise on Geophysics* (pp. 139–159). Elsevier. https://doi.org/10.1016/B978-0-444-53802-4.00073-7

Ueda, T., Obata, M., Di Toro, G., Kanagawa, K., & Ozawa, K. (2008). Mantle earthquakes frozen in mylonitized ultramafic pseudotachylytes of spinel-lherzolite facies. Geology, 36(8), 607–610. https://doi.org/10.1130/G24739A.1

Violay, M., Nielsen, S., Gibert, B., Spagnuolo, E., Cavallo, A., Azais, P., et al. (2014). Effect of water on the frictional behavior of cohesive rocks during earthquakes. *Geology*, *42*(1), 27–30. https://doi.org/10.1130/G34916.1

Violay, M., Di Toro, G., Nielsen, S., Spagnuolo, E., & Burg, J. P. (2015). Thermo-mechanical pressurization of experimental faults in cohesive rocks during seismic slip. *Earth and Planetary Science Letters*, *429*, 1–10. https://doi.org/10.1016/j.epsl.2015.07.054